공학석사학위논문

Development of Point Generation Technique for a Meshless Method

무격자 유동 해석을 위한 질점 생성 프로그램 개발

2016 년 2 월

서울대학교 대학원

기계항공공학부

이재상

Development of Point Generation Technique for a Meshless Method

무격자 유동 해석을 위한 질점 생성 프로그램 개발

지도교수 김규홍

이 논문을 공학석사 학위논문으로 제출함

2016 년 2 월

서울대학교 대학원

기계항공공학부

이재상

이재상의 공학석사 학위논문을 인준함

2016 년 2 월

위 원 장 ____________________

부위원장 ____________________

위　　원 ____________________

Abstract

Development of Point Generation Technique for a Meshless Method

Jae Sang Rhee
School of Mechanical and Aerospace Engineering
The Graduate School

This study aims to develop meshless point generation technique which can be applied to complicated geometry or moving boundary. Unlike the conventional finite volume method, meshless method requires only point system as a computational domain. Therefore Generation of computational domain is relatively easier than conventional FVM.

In this study, meshless point generation technique is developed. For the validation, the results obtained from the meshless method were compared with the results obtained from the conventional FVM. Practical models, such as Space shuttle or Missile, were selected as a validation model.

For the steady calculation, governing equation is Euler equation. And for the unsteady calculation, Euler equation in Arbitrary Lagrangian Eulerian form is selected as governing equation

Meshless method developed by Huh is used for a flow solver. In both meshless method and FVM, AUSMPW+ was used for numerical flux scheme, minmod limiter was used for limiting process and LU-SGS was used for time integration.

From the results, the robustness and the accuracy of meshless point generation technique are verified.

Keywords : Meshless method, Gridless method, Point generation technique, Moving boundary

Student Number : 2014 – 20671

Table of Contents

List of Figures

List of Tables

Chapter 1. Introduction

1.1 Meshless method

A meshless method is a newly suggested computational fluid dynamics (CFD) algorithm in recent year. This method requires only neighboring points of each point which is called local points cloud without using the concept of mesh. Generally, the conventional finite volume method requires a large amount of time for generating mesh for a complex geometry. Therefore it is less restrictive when generating the computational domain for a complicated or moving geometry than mesh based methods.

1.2 Motivation

A meshless method was introduced in 1977 at first. Since then, a variety of Meshless algorithms have been studied by former researchers. Since 2000, meshless algorithms which analyze compressible flow using moving least square method (LSM) have been developed by Katz (2009) [1] respectively and so on.

The ultimate goal of meshless method is to analyze the unsteady compressible flow around multi-bodies which consider 6-DOF (Degree of Freedom) motion. However the previous researchers did not consider all kind of moving such as 6-DOF motion. As part of the development of the ultimate point generation technique, point generation technique for one body which has complicated geometry was developed in this study. Validation models are Space shuttle, NASA X TM2059, moving cylinder and moving sphere. Numerical analysis on the flow around those models are carried out using meshless solver developed by Huh [2], [4]. And those results are compared with the structured finite volume method for validation. In both methods, AUSMPW+, minmod limiter, and LU-SGS are used

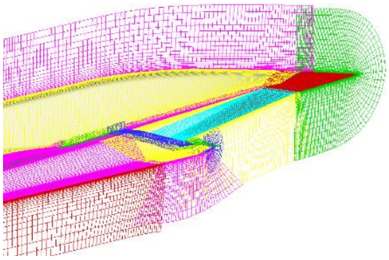

Figure 1 Grid system of X-51 scramjet

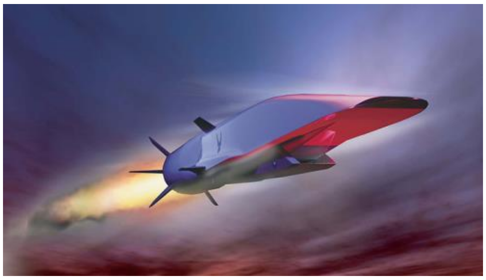

Figure 2 X-51 scramjet with a Pegasus booster

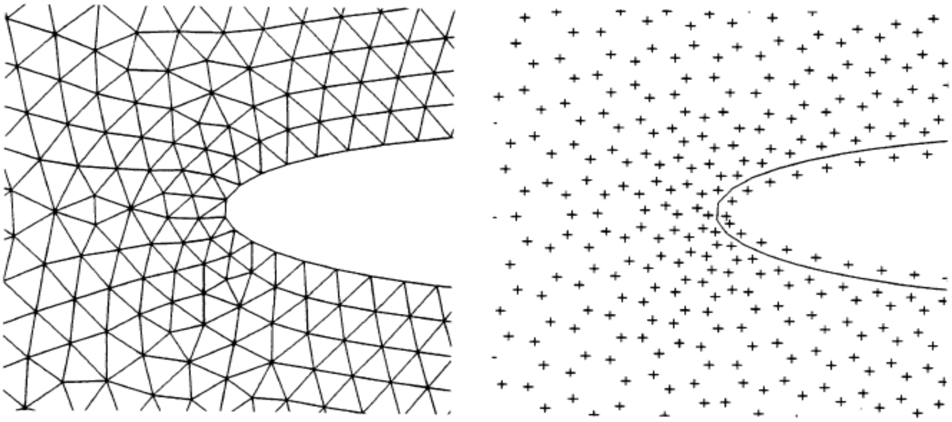

Figure 3 comparison of unstructured grid and meshless points

Chapter 2. Point generation technique

2.1 Meshless point system

The meshless point system consists of two point systems. The first is the near surface point system, and the other is the background point system. The near surface point system is used for boundary layer. Therefore, it is generated along the surface, as shown in Figure 4.

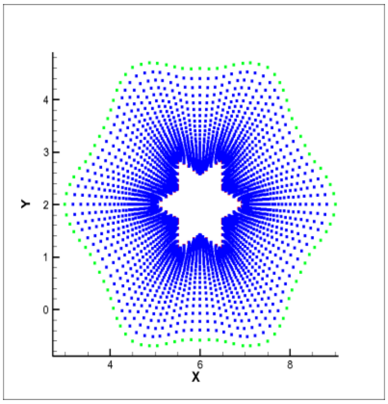

Figure 4 the near surface point system

On the other hand, the background point system is generated outside the near surface point system. And it is created from the Cartesian grid point. As shown in Figure 5

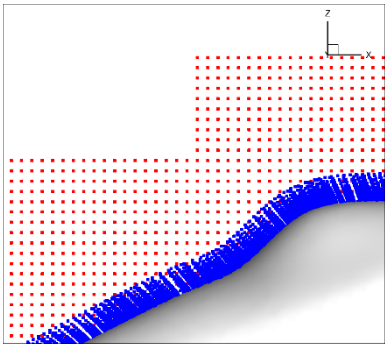

Figure 5 the background point system

2.2 Near surface point system

As explained in chapter 2.1, near surface point system is used to enhance the accuracy of calculation in the boundary layer. In this study, the near surface point system is generated along the Electric field line from the surface. The E-field line is easily computed using surface mesh information using Coulomb's law. It is shown in Eq. (1)

$$E_{x,i} = \sum_j \frac{k_j}{d^{\frac{3}{2}}} (x_{S,j} - x_i)$$

$$E_{y,i} = \sum_j \frac{k_j}{d^{\frac{3}{2}}} (y_{S,j} - y_i)$$

$$E_{z,i} = \sum_j \frac{k_j}{d^{\frac{3}{2}}} (z_{S,j} - z_i) \tag{1}$$

In Eq. (1), $E_{x,i}$, $E_{y,i}$, $E_{z,i}$ are x, y, z component of the electric field at point i which is located outside the surface, $x_{\mathrm{S,j}}$, $y_{\mathrm{S,j}}$, $z_{\mathrm{S,j}}$ are x, y, z-coordinate of the surface mesh point which has index j. And x_i, y_i, z_i are x, y, z-coordinate of the point i, d is the distance between point i and j, and k_j is the constant which is determined by users. The electric field line can be obtained by Eq. (1). Figure 6 shows the generated three dimensional near surface point system of the concave-shaped object.

2.3 Background point system

The background point system is generated from the Cartesian grid point. In order to generate the background point system, three input values are needed in each x, y, z direction. The first is interval of point, the second is coordinate of initial point, and the last is the number of points. From these input values, the coordinates of the background point can be derived, as shown in Eq. (2).

$$\begin{aligned} x_{i,j,k} &= x_{ini} + (i-1)\Delta x, \qquad (1 \leq i \leq N_x) \\ y_{i,j,k} &= y_{ini} + (j-1)\Delta y, \qquad (1 \leq j \leq N_y) \\ z_{i,j,k} &= z_{ini} + (k-1)\Delta z, \qquad (1 \leq k \leq N_z) \end{aligned} \tag{2}$$

In Eq. (2), Δx, Δy Δz denote the interval of point, N_x, N_y, N_z are the number of points, and x_{ini}, y_{ini}, z_{ini} are the coordinates of the initial point. Among the background points, the points which are located in the near surface point system are excluded from the calculation. The total point system is shown in both Figure 7 and Figure 8.

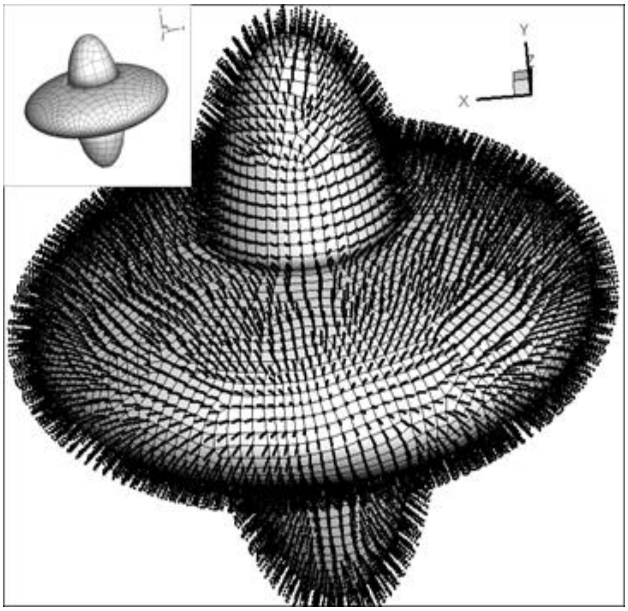

Figure 6 the three dimensional near surface point system

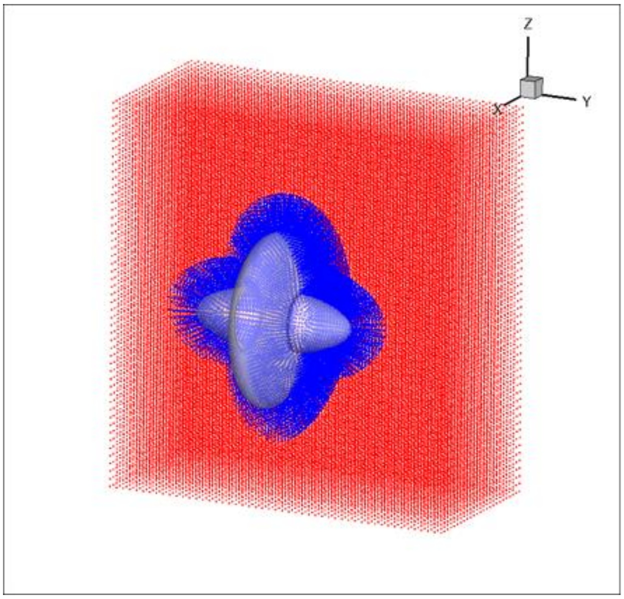

Figure 7 the three dimensional meshless point system

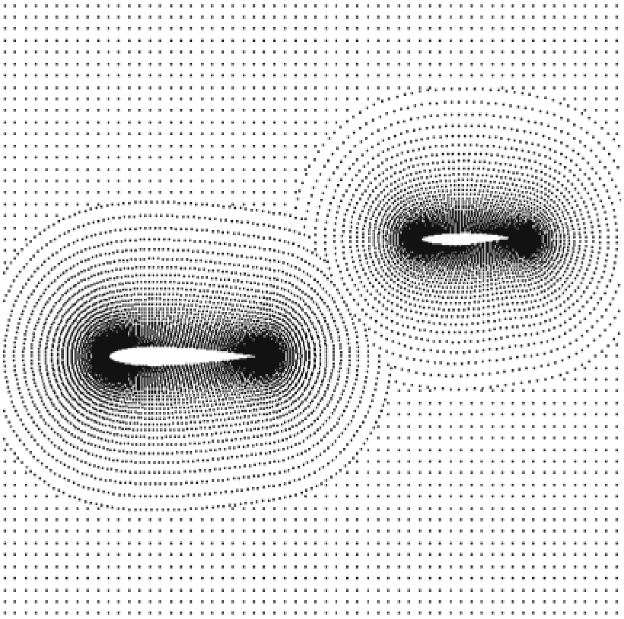

Figure 8 the two dimensional meshless point system

2.4 Local points cloud

Most of computational methods, including finite element method (FEM), finite difference methods (FDM), and finite volume method (FEM), depend on the interlaced grids or finite volumes. In order to discretize PDE, every point require the set of neighboring points not the grid information in meshless scheme. The set of neighboring points is called local points cloud. For the accuracy, the robustness, and the efficiency, appropriate composition of local points cloud is critical. In this paper, the strategy of generation of local points cloud is proposed. The strategy is shown as follows.

2.4.1 Two dimensional local points cloud

In two dimensional space, total 8 points to be chosen for the local points cloud. The criterion for composing the local points cloud is as follows.

- Find the closest point of the central point.
- Divide the region into eight sector equally, which the line between the central point and the closest point is the bisecting line of angle of the sector. As shown in Figure 9.
- Within each sector, the closest point is selected as a point of local cloud.

2.4.2. Three dimensional local points cloud

In three dimensional space, total 18 points constitute the local points cloud. the criterion for composing the local points cloud is as follows.

- Generate virtual cube which has a point as a center.
- Draw square, consist of internal division point between center point and vertex on the face, on each face as show in Figure 10.

- Connect every vertex on the bigger square and the corresponding vertex on the little one
- Then, every face will be split into the five polygon, one square, and four trapezoids.
- If the ratio of internal division is $a:b = (\sqrt{5}+2)/2$ (golden ratio), 18 zones which have same are generated, as shown in Figure 11. The same zone is denoted as same color.
- Find the closest point in each zone, these points constitute the local points cloud.

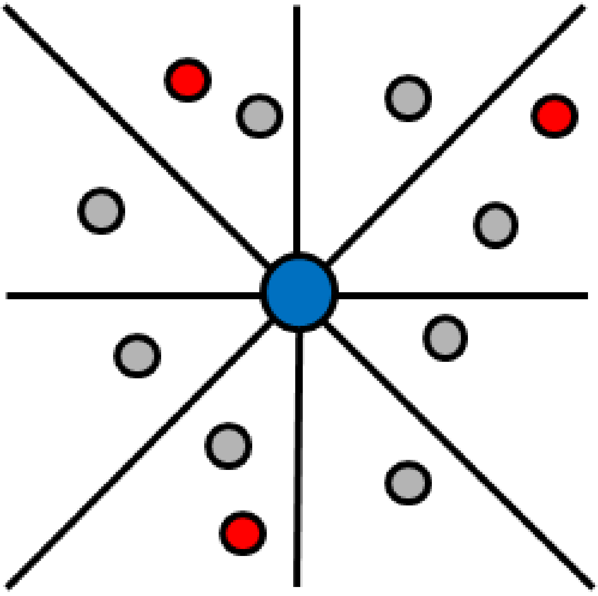

Figure 9 two dimensional cloud shape

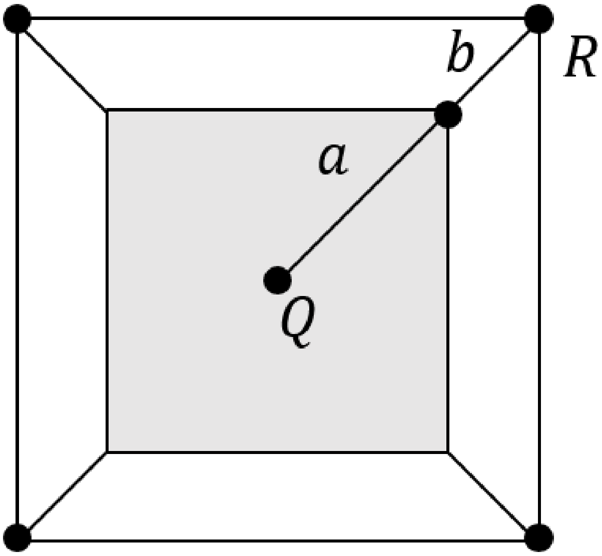

Figure 10 face splitting on cube

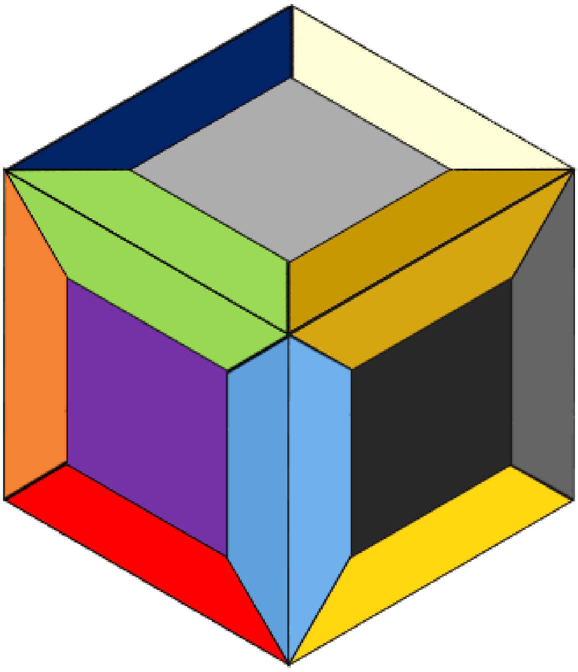

Figure 11 divided region

2.5 Moving principle of points

2.5.1 Moving methodology

When the object moves, the near surface point system moves with same speed of object. On the other hand, the background point system is fixed. Therefore, the near surface point system and the background point system are overlapped, as shown in Figure 13. The overlapped background points must be eliminated for the computation. For the better computational speed, the background point system change their state when the point moves, not being eliminated in this study. For example, when a background point is overlapped, the point is set to ‘OFF’. They can be seen as the red points in Figure 12. Then the point become non-overlapped, the point is set to ‘ON’. They also can be seen as the green points in Figure 13. Figure 13 Shows the regenerated point system for the next physical time step

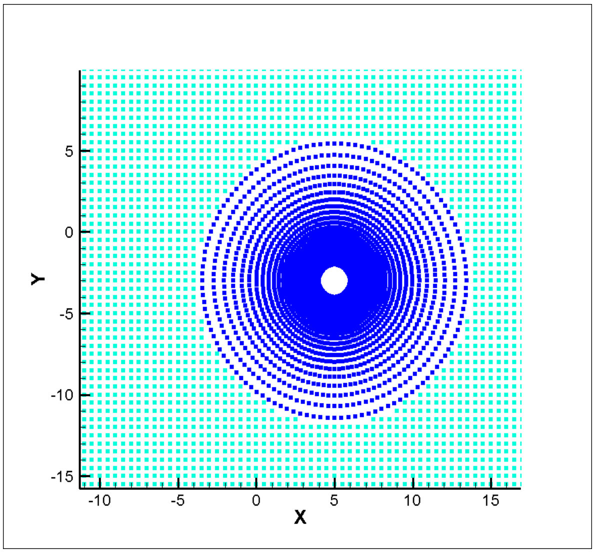

Figure 12 initial point system

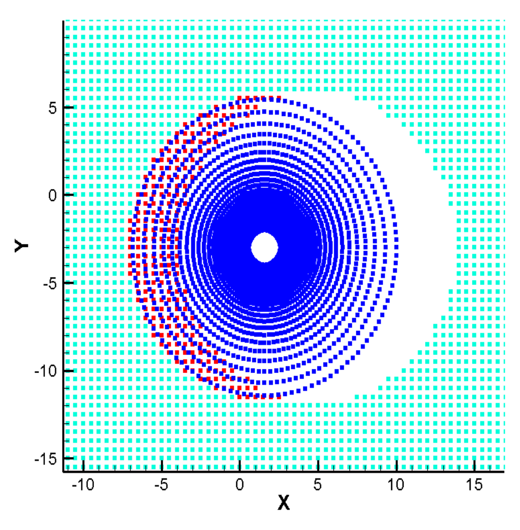

Figure 13 overlapping and vacancy

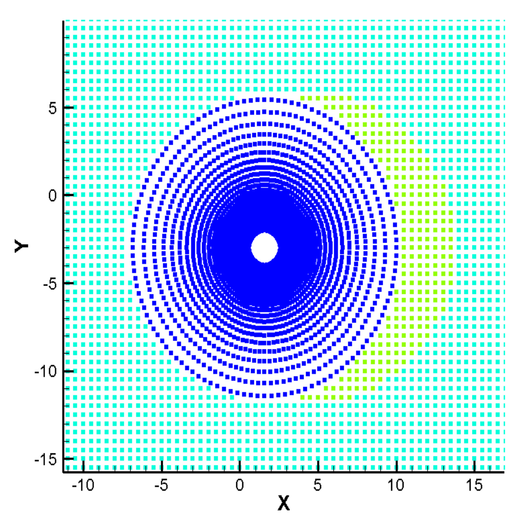

Figure 14 regenerated point system

2.5.2 Sorting point for local point cloud

After the regeneration of the point system, points should constitute their own local points cloud again. However, to constitute local points cloud for all points consumes a lot of time. Therefore, points which constitute new local points cloud unconditionally should be sorted. Except those points, they use their old local points cloud. The sorting strategy is as follows.

- The outmost points of the near surface point system

The outmost points of the near surface point system move with the object. The neighboring points of these points change when the object moves, because the background points are fixed. It is shown in the Figure 15.

- The newly included points due to the movement of the object

As shown in Figure 14, when the object moves, the background points are generated. These points was 'OFF' in the previous physical time step. They don't have local point cloud. Consequently, these points constitute local point cloud.

- The neighboring points of 'OFF' state points

In Figure 13, the overlapped points are denoted as red color. Because those points are excluded from the computational domain, a point which uses those points as a local point cloud lose their connectivity. Therefore, these points should constitute the local point cloud again.

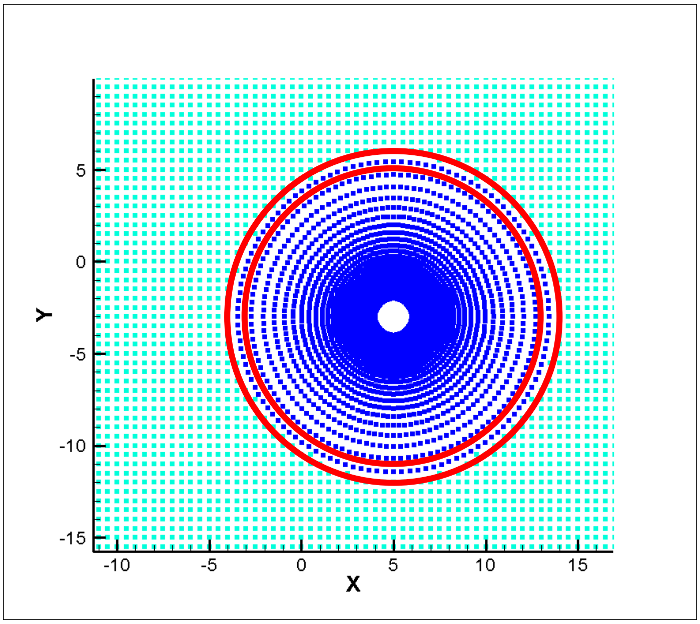

Figure 15 outmost points of the near surface point system

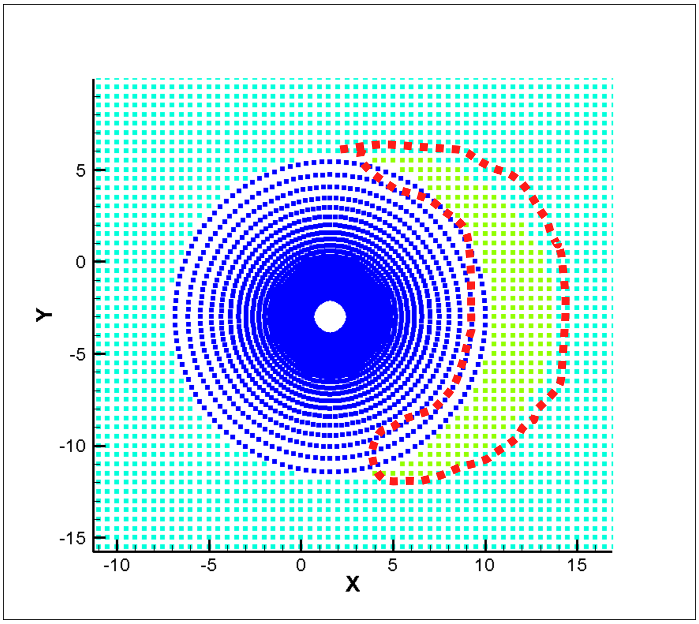

Figure 16 newly included points (green points)

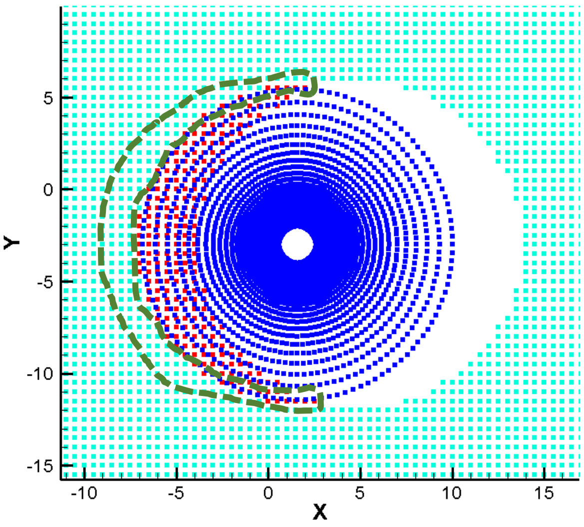

Figure 17 neighboring point of the overlapped points

2.5.2 Strategy : rapid generation of new local point cloud

When a point searching their new local point cloud, to search point for all domain is not desirable. In order to decrease the time for searching, two strategies are established. The first is for the outmost points of the near surface point system, and the other is for the background point system. Methodology is as follows.

- Outmost points

The outmost points have their own block information. Block information means that Cartesian ‘I’ and ‘J’ index of the background point which exists upper-left corner to the outmost point and this point called ‘*background block point*’. Additionally, the background number of the background block point is required. This number is called ‘N’. These are shown in the Figure 18. Using given information, the existing background points which have Cartesian index ‘I’ or ‘I+1’ or ‘I-1’, and index ‘J’ or ‘J+1’ or ‘J-1’ are the candidates of local point cloud. Then, in the old local point cloud, the point which is the near surface point is used again. It is denoted as color dot in Figure 18.

- Background points

Using Cartesian ‘I’ and ‘J’ index of the background point, the existing background points which have Cartesian index ‘I’ or ‘I+1’ or ‘I-1’, and index ‘J’ or ‘J+1’ or ‘J-1’ are the candidates of local point cloud. Then the outmost points of the near surface point system are selected for candidate. It is shown in Figure 19

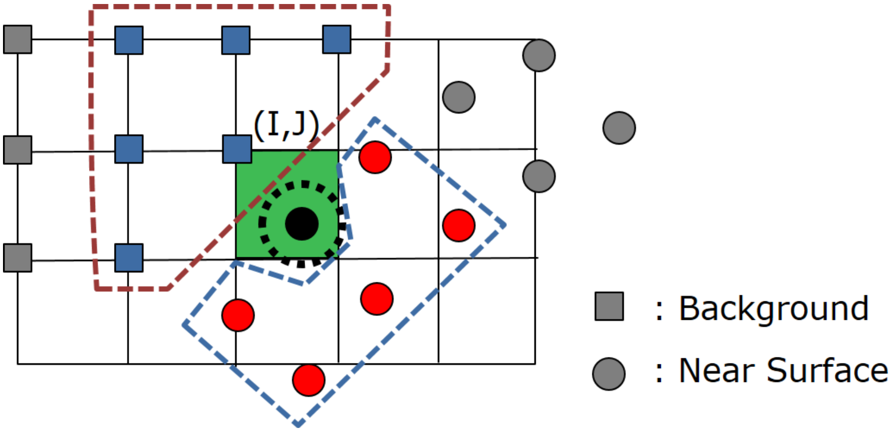

Figure 18 indicating the candidates of local point cloud (near surface point)

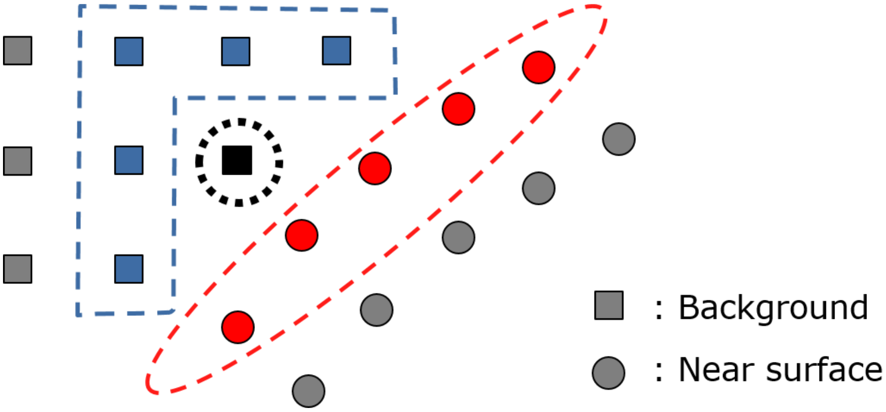

Figure 19 indicating the candidates of local point cloud (background point)

Chapter 3. Numerical Method

3.1 Governing Equation

3.1.1 Euler equation

For a non-equilibrium and inviscid gas, the governing equation is a three-dimensional Euler equation which considering species continuity and vibrational energy equation. The equation is as follows.

$$\frac{\partial U}{\partial t}+\frac{\partial F}{\partial x}+\frac{\partial G}{\partial y}+\frac{\partial H}{\partial z}=S \tag{3}$$

Where,

$$U=\begin{bmatrix}\rho\\ \rho u\\ \rho v\\ \rho w\\ E\\ \rho_i\\ \vdots\\ \sum \rho e_{vib,i}\end{bmatrix},\ F=\begin{bmatrix}\rho u\\ \rho u^2+p\\ \rho uv\\ \rho uw\\ (E+p)u\\ \rho_i u\\ \vdots\\ \sum \rho e_{vib,i}u\end{bmatrix}$$

$$G=\begin{bmatrix}\rho v\\ \rho uv\\ \rho v^2+p\\ \rho wv\\ (E+p)v\\ \rho_i v\\ \vdots\\ \sum \rho e_{vib,i}v\end{bmatrix},H=\begin{bmatrix}\rho w\\ \rho uw\\ \rho vw\\ \rho w^2+p\\ (E+p)w\\ \rho_i w\\ \vdots\\ \sum \rho e_{vib,i}w\end{bmatrix},S=\begin{bmatrix}0\\ 0\\ 0\\ 0\\ W_i\\ \vdots\\ \sum W_{vib,i}\end{bmatrix}, \tag{4}$$

S is source term that includes $\mathrm{W_i}$ in the species continuity equations and $\mathrm{W_{vib,i}}$ in the vibrational energy equation which are calculates according to Ref. [6] and [7].

3.1.2. Euler eqation in Arbitrary Lagrangian Eulerian form

An appropriate choice of *kinematic description* is primarily important consideration when simulating unsteady problems. However, purely Lagrangian and purely Eulerian descriptions have demerits, a technique, combining the best features of both descriptions, has been developed. Such a technique is called Arbitrary Lagrangian Eulerian (ALE) description. In Lagrangian description, the computational nodes are moved with the continuum. Then, in Eulerian description, the computational nodes are held in fixed. On the other hand, in ALE description, the computational nodes are moved with arbitrary speed [8]. And Euler equation in ALE form is shown as follows.

$$\frac{\partial U}{\partial t}+\frac{\partial F}{\partial x}+\frac{\partial G}{\partial y}+\frac{\partial H}{\partial z}=S \tag{5}$$

Where,

$$U=\begin{bmatrix}\rho\\ \rho u\\ \rho v\\ \rho w\\ E\end{bmatrix},\ F=\begin{bmatrix}\rho(u-\hat{u})\\ \rho u(u-\hat{u})+p\\ \rho v(u-\hat{u})\\ \rho w(u-\hat{u})\\ E(u-\hat{u})+pu\end{bmatrix},$$

$$G=\begin{bmatrix}\rho(v-\hat{v})\\ \rho u(v-\hat{v})\\ \rho v(v-\hat{v})+p\\ \rho w(v-\hat{v})\\ E(v-\hat{v})+pv\end{bmatrix},H=\begin{bmatrix}\rho(w-\hat{w})\\ \rho u(w-\hat{w})\\ \rho v(w-\hat{w})\\ \rho w(w-\hat{w})+p\\ E(w-\hat{w})+pw\end{bmatrix} \tag{6}$$

In Eq. (6), $\hat{u}$, $\hat{v}$, $\hat{w}$ denote the velocity component of points *x*, *y*, *z* direction respectively.

3.2 Least square method

In the meshless method, least square method based on Taylor series expansion has been used to discretize PDE. Given a function $\phi(\chi)$ with $\chi = (x, y, z)$ in three dimension, the Taylor expansion from the point cloud center (x_0, y_0, z_0) is denoted as

$$\phi(x,y,z) = \Delta x \frac{\partial\phi(x_0)}{\partial x} + \Delta y \frac{\partial\phi(y_0)}{\partial y} + \Delta z \frac{\partial\phi(z_0)}{\partial z} + O(\Delta^2) \tag{7}$$

The least square method with weighted function may be expressed as follows.

$$\min \sum_{j=1}^{n} \omega_{0j} \left[\Delta\phi_{0j} - \Delta x \frac{\partial\phi(x_0)}{\partial x} - \Delta y \frac{\partial\phi(y_0)}{\partial y} - \Delta z \frac{\partial\phi(z_0)}{\partial z}\right]^2 \tag{8}$$

$$\frac{\partial\phi}{\partial x} \approx \sum_j a_{0j}(\phi_j - \phi_0) \tag{9}$$

$$\frac{\partial\phi}{\partial y} \approx \sum_j b_{0j}(\phi_j - \phi_0) \tag{10}$$

$$\frac{\partial\phi}{\partial z} \approx \sum_j c_{0j}(\phi_j - \phi_0) \tag{11}$$

In Eq. (8), j is an index of point in the local point cloud and n is the number of points in the cloud.

In a three dimensional case, the matrix equation which derives least square coefficient a_{0j}, b_{0j}, c_{0j} is as follows.

$$AX = B \tag{12}$$

Where,

$$X^T = [a_k, b_k, c_k] \tag{13}$$

$$A = \begin{bmatrix} \Sigma\omega\Delta x^2 & \Sigma\omega\Delta x\Delta y & \Sigma\omega\Delta x\Delta z \\ \Sigma\omega\Delta x\Delta y & \Sigma\omega\Delta y^2 & \Sigma\omega\Delta y\Delta z \\ \Sigma\omega\Delta x\Delta z & \Sigma\omega\Delta y\Delta z & \Sigma\omega\Delta z^2 \end{bmatrix} \tag{14}$$

$$B^T = [\Sigma\omega\Delta x\Delta\varphi, \Sigma\omega\Delta y\Delta\varphi, \Sigma\omega\Delta z\Delta\varphi] \tag{15}$$

Solving Eq. (12), the solution is as follows.

$$a_k = \frac{M_{11}}{|A|}\sum \omega\Delta x\Delta\varphi + \frac{M_{12}}{|A|}\sum \omega\Delta y\Delta\varphi + \frac{M_{13}}{|A|}\sum \omega\Delta z\Delta\varphi \tag{16}$$

$$b_k = \frac{M_{21}}{|A|}\sum \omega\Delta x\Delta\varphi + \frac{M_{22}}{|A|}\sum \omega\Delta y\Delta\varphi + \frac{M_{23}}{|A|}\sum \omega\Delta z\Delta\varphi \tag{17}$$

$$c_k = \frac{M_{31}}{|A|}\sum \omega\Delta x\Delta\varphi + \frac{M_{32}}{|A|}\sum \omega\Delta y\Delta\varphi + \frac{M_{33}}{|A|}\sum \omega\Delta z\Delta\varphi \tag{18}$$

Where,

$$|A| = \sum \omega\Delta x^2 \sum \omega\Delta y^2 \sum \omega\,\Delta z^2$$

$$\left[1 - \frac{(\sum \omega\Delta x\Delta z)^2}{\sum \omega\Delta x^2 \sum \omega\Delta z^2} - \frac{(\sum \omega\Delta x\Delta y)^2}{\sum \omega\Delta y^2 \sum \omega\Delta x^2} - \frac{(\sum \omega\Delta y\Delta z)^2}{\sum \omega\Delta z^2 \sum \omega\Delta y^2}\right]$$

$$+2[\sum \omega\Delta x\Delta y \sum \omega\Delta y\Delta z \sum \omega\Delta x\Delta z] \tag{19}$$

$$M_{11} = \sum \omega\Delta y^2 \sum \omega\Delta z^2 - \left(\sum \omega\Delta y\Delta z\right)^2 \tag{20}$$

$$M_{12} = \sum \omega\Delta x\Delta z \sum \omega\Delta y\Delta z - \sum \omega\Delta x\Delta y \sum \omega\Delta z^2 \tag{21}$$

$$M_{13} = \sum \omega\Delta x\Delta y \sum \omega\Delta y\Delta z - \sum \omega\Delta x\Delta z \sum \omega\Delta y^2 \tag{22}$$

$$M_{21} = \sum \omega\Delta y\Delta z \sum \omega\Delta x\Delta z - \sum \omega\Delta x\Delta y \sum \omega\Delta z^2 \tag{23}$$

$$M_{22} = \sum \omega\Delta x^2 \sum \omega\Delta z^2 - \left(\sum \omega\Delta x\Delta z\right)^2 \tag{24}$$

$$M_{23} = \sum \omega\Delta x\Delta z \sum \omega\Delta x\Delta y - \sum \omega\Delta y\Delta z \sum \omega\Delta x^2 \tag{25}$$

$$M_{31} = \sum \omega\Delta x\Delta y \sum \omega\Delta y\Delta z - \sum \omega\Delta x\Delta z \sum \omega\Delta y^2 \tag{26}$$

$$M_{32} = \sum \omega\Delta x\Delta y \sum \omega\Delta x\Delta z - \sum \omega\Delta y\Delta z \sum \omega\Delta x^2 \tag{27}$$

$$M_{33} = \sum \omega\Delta x^2 \sum \omega\Delta y^2 - \left(\sum \omega\Delta x\Delta y\right)^2 \tag{28}$$

3.3 Spatial Discretization

3.3.1 AUSMPW+ for meshless method

The AUSMPW+ scheme [9] is used for chemically reactive flow, i.e. equilibrium and non-equilibrium flow.

The main feature of AUSMPW+ is to remove oscillations of AUSM+ near wall or across a strong while maintain the accuracy of the original scheme. In this study, AUSMPW+ modified for the meshless scheme is used. Ignoring source term and three dimensional term, Eq. (3) can be simply expressed as

$$\frac{\partial U_i}{\partial t} + \sum_{j=1}^{n} a_{ij}\Delta f_{ij} + \sum_{j=1}^{n} a_{ij}\Delta f_{ij} + \sum_{j=1}^{n} b_{ij}\Delta g_{ij} = 0 \qquad (29)$$

Then,

$$\frac{\partial U_i}{\partial t} + \sum_{j=1}^{n} \Delta\mathcal{F}_{ij} = 0 \qquad (30)$$

In Eq. (30), $\mathcal{F} = \mathrm{af} + \mathrm{bg}$ is a directed flux along the metric weight vector (a, b). Because AUSMPW+ scheme uses mid flux at j+1/2 instead of the flux at j, Eq. (30) can be expressed as follows [10].

$$\sum_{j=1}^{n} \Delta\mathcal{F}_{ij} = 2\sum_{j=1}^{n} \Delta\mathcal{F}_{ij+\frac{1}{2}} = 2\sum_{j=1}^{n} (\mathcal{F}_{ij+\frac{1}{2}} - \mathcal{F}_{ij}) \qquad (31)$$

The numerical flux of AUSMPW+ is given by

$$\mathcal{F}_{\frac{1}{2}} = \bar{M}_L^{+} c_{\frac{1}{2}} \Phi_L + \bar{M}_R^{-} c_{\frac{1}{2}} \Phi_R + (P_L^{+} P_L + P_R^{-} P_R) \qquad (32)$$

$\Phi = (\rho, \rho\mathrm{u}, \rho\mathrm{H})^{\mathrm{T}}$ and $\mathrm{P} = (0, \mathrm{p}, 0)^{\mathrm{T}}$. The subscripts 1/2 and (L,R) stand for a quantity at a midpoint on the edge of Figure 20 and the left and the right states across the edge, respectively. The Mach number at midpoint is defined as

$$m_{\frac{1}{2}} = M_L^+ + M_R^- \tag{33}$$

When $\bar{\mathrm{M}}_{\mathrm{L}}^{+}$ and $\bar{\mathrm{M}}_{\mathrm{R}}^{-}$ are given as follows.

i) $m_{\frac{1}{2}} = M_L^+ + M_R^0 \geq 0, \text{then}$

$$\bar{M}_L^+ = M_L^+ + M_R^-[(1-w)(1+f_R) - f_L] \tag{34}$$

$$\bar{M}_R^- = w(1+f_R) \tag{35}$$

i) $m_{\frac{1}{2}} = M_L^+ + M_R^0 < 0, \text{then}$

$$\bar{M}_L^+ = M_L^+ + w(1+f_L) \tag{36}$$

$$\bar{M}_R^- = M_R^- + M_L^+[(1-w)(1+f_L) - f_R] \tag{37}$$

In Eq. (34)~(37), w does not mean the z-directional velocity. w is given as follows.

$$w(P_L, P_R) = 1 - min\left(\frac{P_L}{P_R}, \frac{P_R}{P_L}\right)^3 \tag{38}$$

The pressure-based weight function is simplified to

$$f_{L,R} = \left(\frac{P_{L,R}}{P_s} - 1\right), P_s \neq 0 \tag{39}$$

Where

$$P_s = P_L^+ P_L + P_R^- P_R \tag{39}$$

The split Mach number is defined by

$$M^{\pm} = \begin{cases} \pm\frac{1}{4}(M \pm 1)^2, & |M| \leq 1 \\ \frac{1}{2}(M \pm |M|), & |M| > 1 \end{cases} \tag{40}$$

$$P^{\pm} = \begin{cases} \pm\frac{1}{4}(M \pm 1)^2(2 \mp M), & |M| \leq 1 \\ \frac{1}{2}(1 \pm sign(M)), & |M| > 1 \end{cases} \tag{41}$$

The Mach number of each side is

$$M_{L,R} = \frac{U_{L,R}}{C_{1/2}} \tag{42}$$

And the speed of sound $c_{1/2}$ is

$$c_{1/2} = \begin{cases} min\left(\frac{c^{*2}}{max(|U_L|, c^*)}\right), & \frac{1}{2}(U_L + U_R) > 0 \\ min\left(\frac{c^{*2}}{max(|U_R|, c^*)}\right), & \frac{1}{2}(U_L + U_R) < 0 \end{cases} \tag{43}$$

Where

$$c^* = \sqrt{2(\gamma - 1)/(\gamma + 1)H_{normal}} \tag{44}$$

$$H_{normal} = \frac{1}{2}\left(H_L - \frac{1}{2}V_L^2 + H_R - \frac{1}{2}V_R^2\right) \tag{45}$$

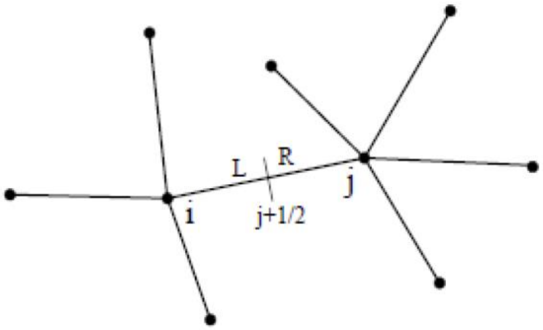

Figure 20 illustration of mid-point value on the edge connecting nodes *i* and *j*

3.3.2 Minmod limiter for meshless method

To improve accuracy, TVD scheme is adopted to the meshless scheme. In this study, minmod limiter [11] is used at AUSMPW+. The basic form of spatial interpolation is given by

$$\Phi_L = \Phi_i + 0.5\phi_L(\Phi_j - \Phi_i) \tag{46}$$

$$\Phi_R = \Phi_j + 0.5\phi_R(\Phi_i - \Phi_j) \tag{47}$$

In order to apply to meshless method, it is necessary to modify minmod limiter as follows.

$$\phi = max(0, min(1, r_k)) \tag{48}$$

Where $k \in \{\text{local point cloud of node } i \; \& \; \theta_{kij} \; is \; max\}$

$$r_k = \frac{s_{ik'}}{s_{ji}} = \frac{s_{ki}}{s_{ji}} cos(\theta_{kij}) \tag{49}$$

$$s_{ki} = \frac{\Phi_k - \Phi_i}{\|\overrightarrow{x_k} - \overrightarrow{x_i}\|} \tag{50}$$

Since there is no point on the opposite side of point j in the vicinity of point i in general point system, nearest point k to the opposite side is used to calculate r_k shown in Figure 21.

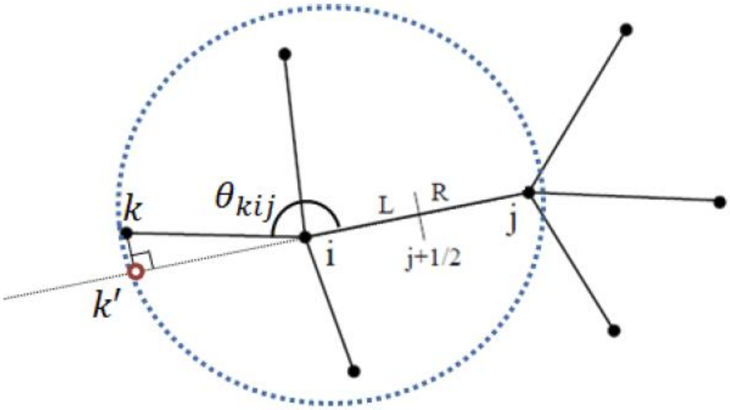

Figure 21 minmod limiter for the meshless method

3.4 Time Integration

Referring to the works of Yoon [12], and Chen [13], LU-SGS is adopted to the meshless method. By applying Eq. (30) and Eq. (31), Euler equation can be rewritten in a semi-discrete form as follows.

$$\frac{\partial U_i^{n+1}}{\partial t} + 2\sum_{j=1}^{n}(F_{ij}^{n+1} - F_i^{n+1}) = S_i^n \tag{51}$$

The flux function F_{ij}^{n+1} may be linearized by setting

$$F_{ij}^{n+1}(\omega_i, \omega_j) \approx F_{ij}^n + A_{ij}^+(\omega_i)\delta\omega_i + A_{ij}^-(\omega_j)\delta\omega_j \tag{52}$$

When n is the time level and matrices $A_{ij}^{\pm}$ are constructed as follows

$$A_{ij}^{\pm} = \frac{1}{2}(A_{ij} \pm \lambda_{ij} I) \tag{53}$$

Where,

$$\lambda_{ij} \geq max(|\lambda_A|) \tag{54}$$

Here, λ_A represents eigenvalues of Jacobian matrix.

Using Eq. (52) ~ (54), Eq. (51) can be LU decomposed, the result is as follows.

$$\left(\frac{1}{\Delta t} + \sum_j k|\rho|\right)\Delta U_i + \sum_{j\in LC} 2A^-\Delta U_j + \sum_{j\in UC} 2A^-\Delta U_j - \sum_j A\Delta U_i = -RES \tag{55}$$

In Eq. (55), LC denotes lower cloud in the cloud index, and UC denotes upper cloud in the cloud index.

3.5 Dual-time stepping for meshless method

For time-accurate unsteady analysis, pseudo-time sub iteration strategy is adopted to solve the unsteady problems.

$$\frac{\partial Q}{\partial t} = -\hat{R} \tag{56}$$

The time derivative term is differenced using a backward second-order there point implicit formula and moved to the right-hand side of the equation:

$$0 = -\frac{1.5Q^{n+1} - 2Q^{n} + 0.5Q^{n-1}}{\Delta t} - \hat{R}^{n+1} \tag{57}$$

A pseudo-time derivative of Q is added on the left-hand side of Eq. (37)

$$\begin{aligned} \frac{\partial Q^{n+1}}{\partial \tau} &= -\frac{1.5Q^{n+1} - 2Q^{n} + 0.5Q^{n-1}}{\Delta t} - \hat{R}^{n+1} \\ &= -\hat{R}^{n+1} - \hat{S}^{n+1} \end{aligned} \tag{58}$$

The pseudo-time derivative term is discretized using the first-order Euler implicit formula.

$$\frac{Q^{n+1,m+1} - Q^{n+1,m}}{\Delta \tau} = -\hat{R}^{n+1,m+1} - \hat{S}^{n+1,m+1} \tag{59}$$

Where, a superscript m denotes the pseudo-time iteration level.

The dual-time steeping method adopted here has a second order time accuracy. Then, Eq. (59) can be written as

$$\left[\frac{1}{\Delta \tau} I + \left\{\frac{\partial \hat{R}}{\partial Q} + \frac{\partial \hat{S}}{\partial Q}\right\}^{n+1,m}\right] \Delta Q^{n+1,m} = -\hat{R}^{n+1,m} - \hat{S}^{n+1,m} \tag{60}$$

Chapter 4. Numerical Analysis

4.1 Steady problems

4.1.1 Space shuttle reentry simulation

The first validation case is Space shuttle reentry simulation. Space shuttle has a highly complex geometry. And the flow condition is also highly extreme. The angle of attack is 40 Degree, and the Mach number is 20. The three cases had been conducted for the validation. The first case is the result from the meshless solver based on the meshless point system (MPS) generated from the meshless point generation technique. And the second is the result obtained from the finite volume method, using the structured grid (SG). Lastly, the third case is the result obtained from the meshless solver, using the structured grid point (SGP). The flow condition is shown in the table 1. And the Figure 22 and the Figure 23 show the meshless point system and the structured grid for Space shuttle respectively. Both methods use AUSMPW+ as spatial discretization, and minmod limiter is chosen as a limiting process. For a time integration, LU-SGS is used.

Altitude (Km)	60
Pressure (Pa)	22.461
Temperature (K)	255.77
Ma	20
Angle of attack (Degree)	40
Species (non-equilibrium)	5 (N, O, NO, N2, O2)

Table 1 the flow conditions (Space shuttle reentry)

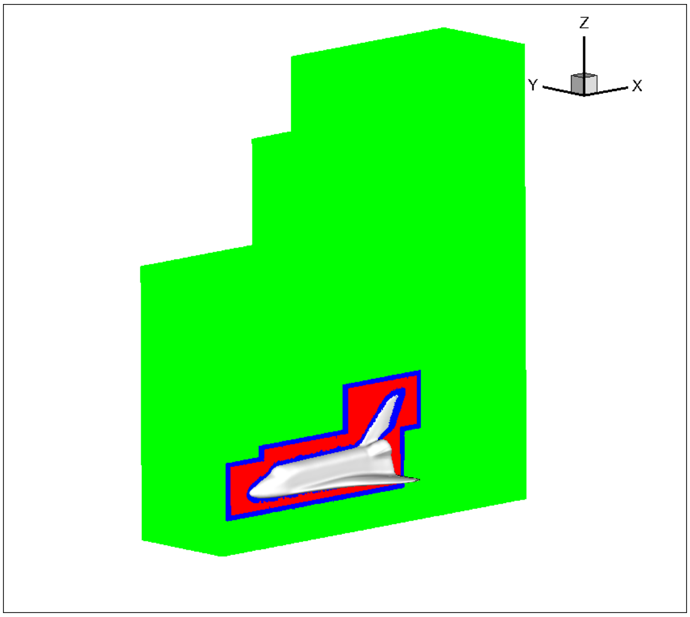

Figure 22 meshless point system (Space shuttle)

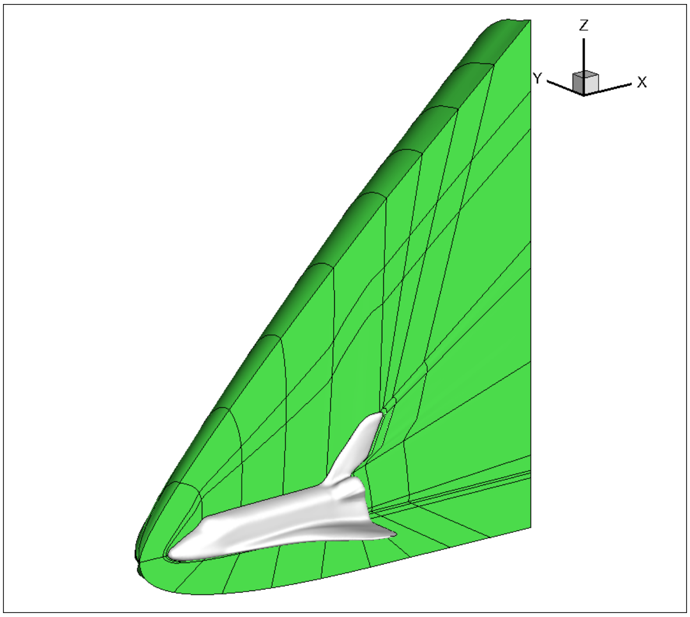

Figure 23 structured grid (space shuttle)

Figure 24, 25, 26 denote results which show the pressure contour. Figure 24 shows the result obtained from the meshless analysis carried on the MPS. Then Figure 25 shows that of FVM. Lastly Figure 26 is the result obtained from the meshless solver based on the SGP.

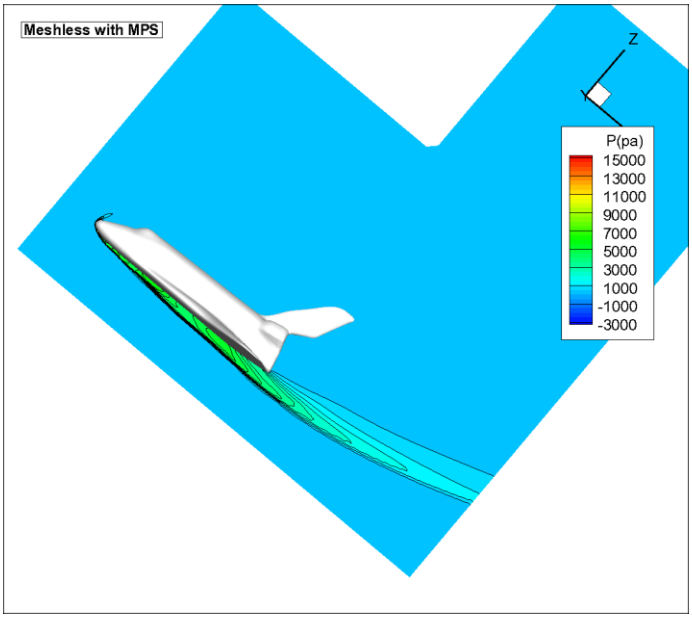

Figure 24 meshless result with MPS

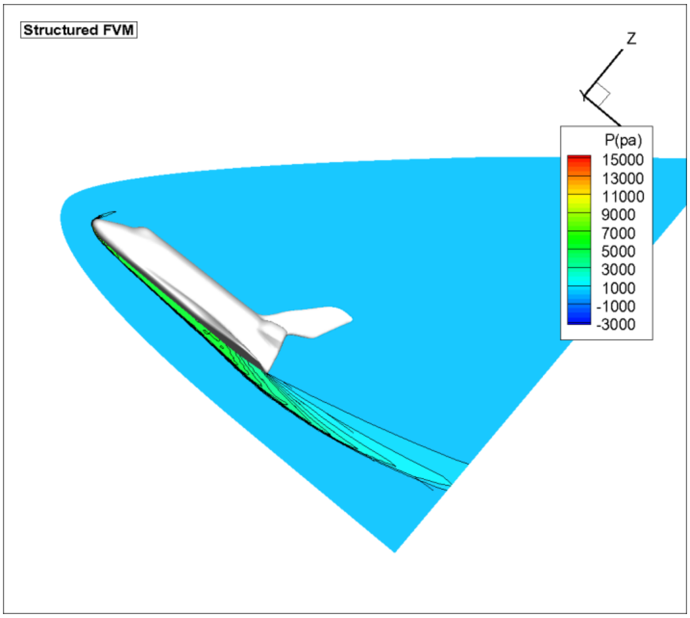

Figure 25 FVM result with SG

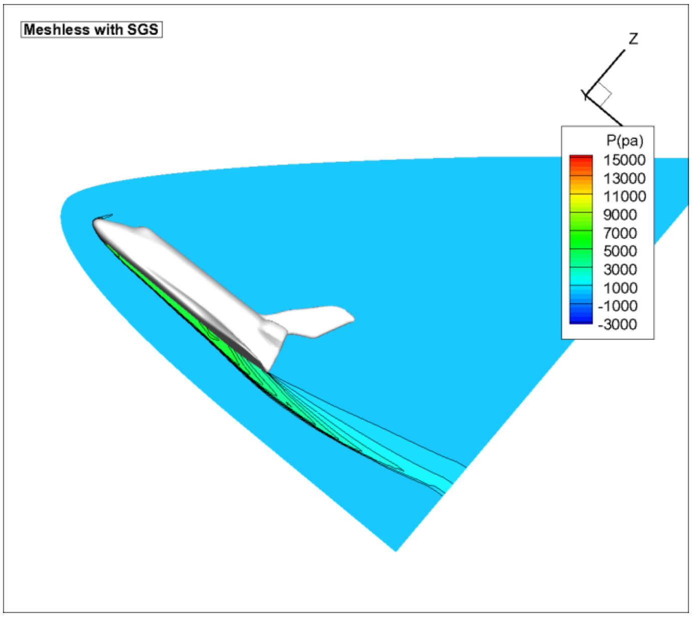

Figure 26 FVM result with SGP

Figure 27 and 28 show the pressure contour at x=300. Figure 27 is the comparison of two solvers on the same computational domain. The left is the result obtained from the meshless method calculated on the SGP. And the right is that of the structured finite volume method. And Figure 28 shows the meshless results which are calculated on the different point systems, SGP and MPS. The left figure is same as the left contour in Figure 27. And the right contour denotes the meshless result using MPS. and the Figure 29 shows the comparison of the pressure coefficient along the surface. The, Table 2 denotes the comparison of the aerodynamic coefficients.

From those results, though the meshless method requires the short time for pre-process, the meshless method has almost same level of accuracy, compared with FVM.

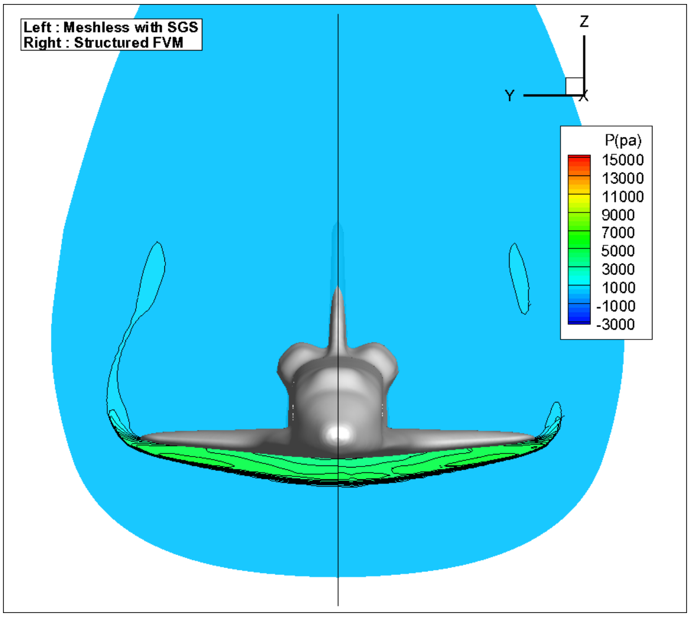

Figure 27 the comparison of the results on the same computational domain(Left : meshless, Right : FVM)

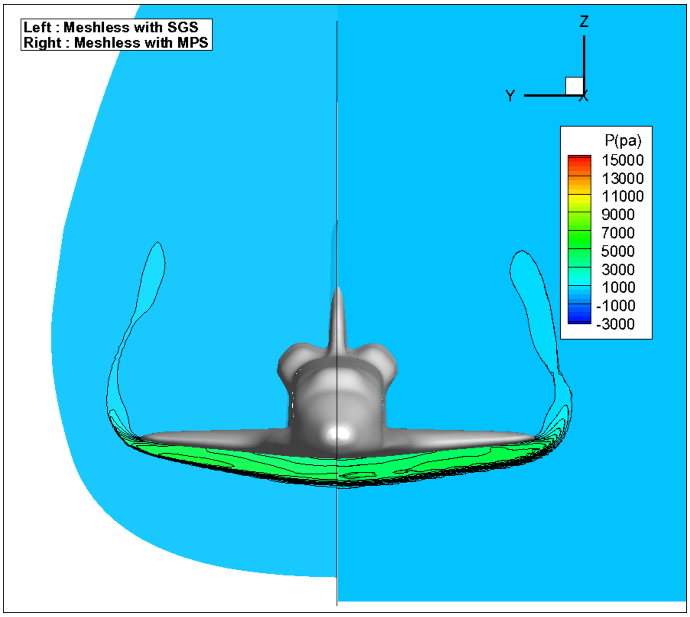

Figure 28 the comparison of the meshless results on the different computational domain(Left : SGP, Right : MPS)

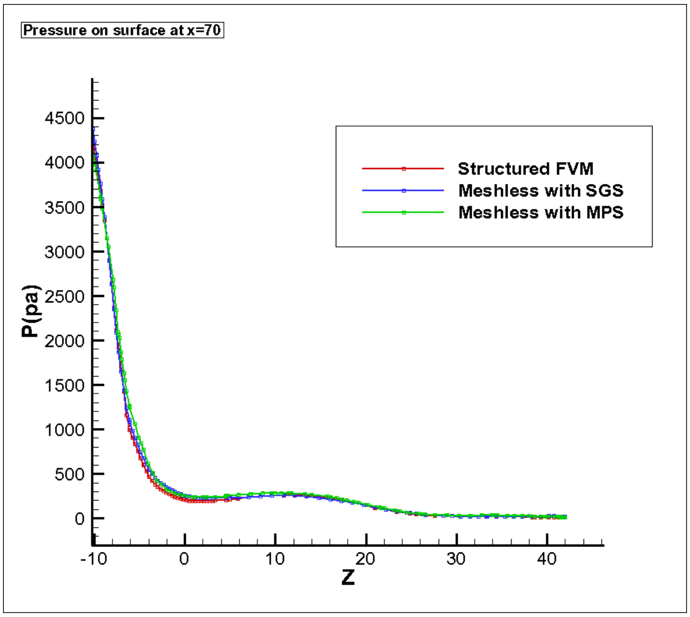

Figure 29 the comparison of pressure coefficient

	SG FVM	SGP meshless	MPS meshelss
C_D	0.585	0.590	0.579
error	-	0.84%	1.08%
C_L	0.751	0.758	0.748
error	-	0.93%	0.47%
L/D	1.284	1.285	1.292
error	-	0.05%	0.60%

Table 2 the comparison of the aerodynamic coefficients

4.1.2 NASA TM X 2059

An analysis on the flow around a highly complicated geometry is the one of the main goals. In order to generate such a model, the modified NASA TM X 2059 model [14] is selected as a next validation model. Four tail fins, the twenty-degree conical nozzle [15] and four vanes are added added to the model. Consequently, this model integrates the internal flow and the external flow. In Figure 32, the generated model is shown.

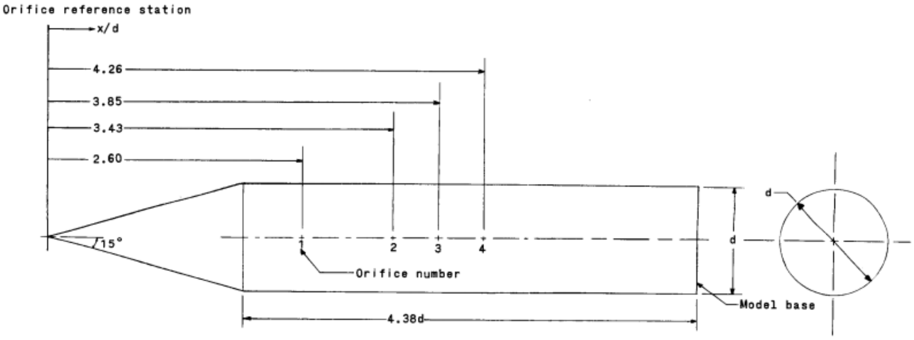

Figure 30 the configuration of NASA TM X 2059

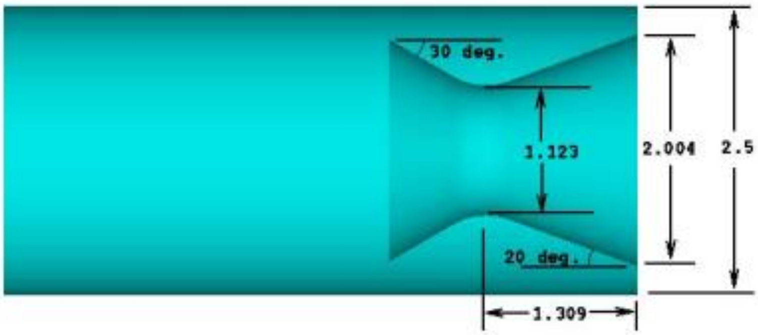

Figure 31 the twenty-degree conical nozzle

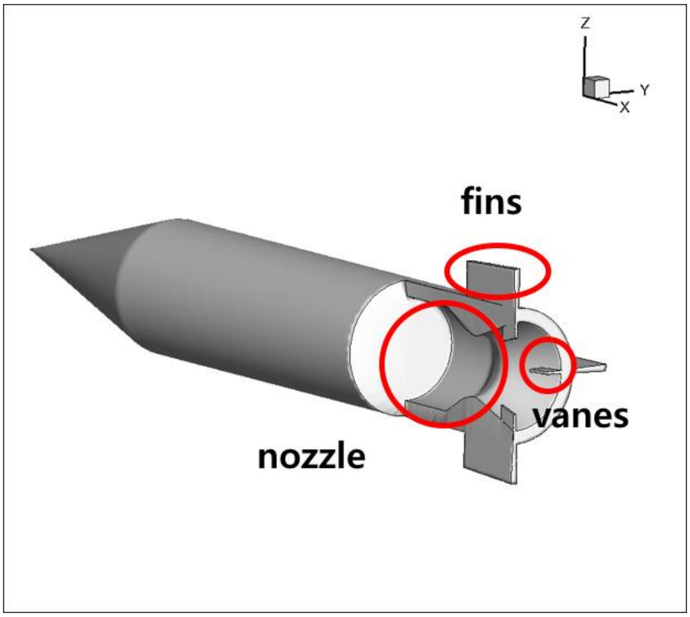

Figure 32 the modified NASA TM X 2059

For a validation, 2 spices flow is analyzed. The freestream flow is air and the nozzle flow is plume. Its freestream conditions are at altitude 10 km and the Mach number is 5. The flow conditions are shown in Table 3. And the meshless point system for the model is shown in Figure 33. For a spatial discretization, AUSMPW+ was used, and as a limiting process, minmod limiter was selected. LU-SGS was selected as a time integration method.

Altitude (km)	10
Pressure (Pa)	26,500
Temperature (K)	223.25210
Mach number	5
Angle of attack (Degree)	0
Spices	Air

Table 3 flow conditions (the modified NACA TM X 2059)

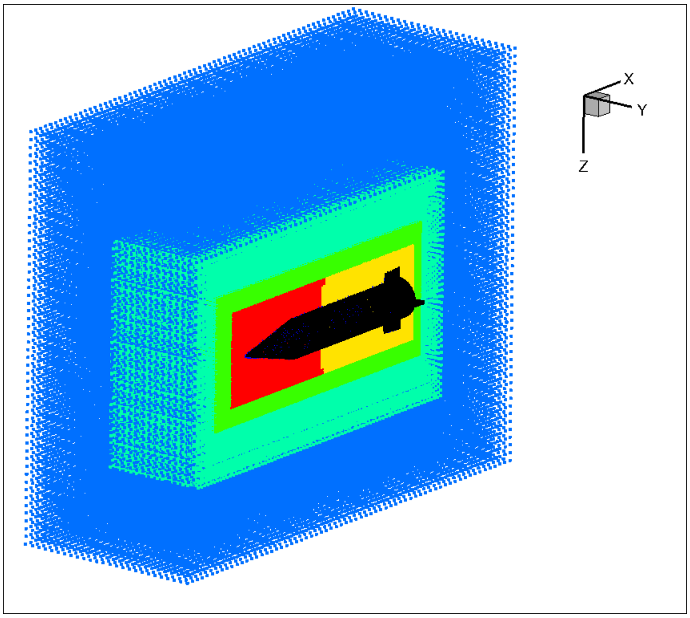

Figure 33 the computational domain for the second validation

Figure 34 ~ 35 show the results and Figure 36 shows the convergence history. Figure 35 shows that 2 spices flows are successfully analyzed.

From the figure 34 ~ 36, no matter how geometry is complicated, the generation technique is available. Consequently, the robustness of the meshless point generation technique and the meshless method was verified.

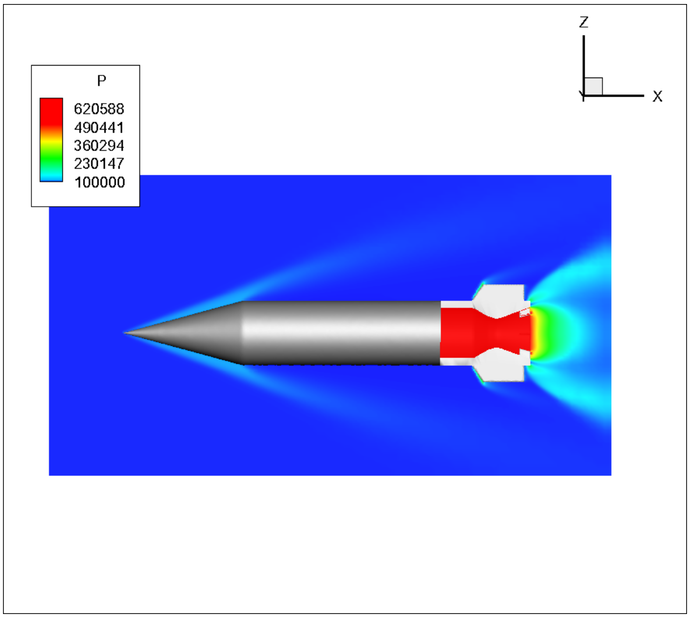

Figure 34 pressure contour (y=0)

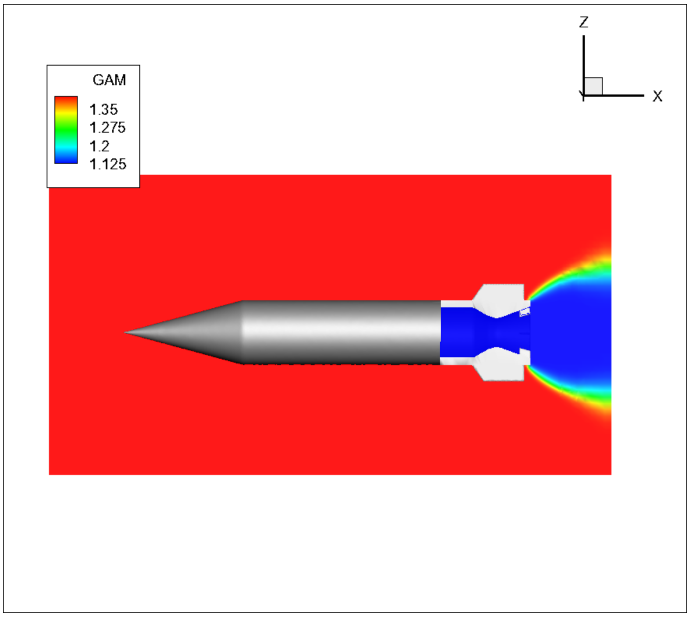

Figure 35 heat of ratio contour (y=0)

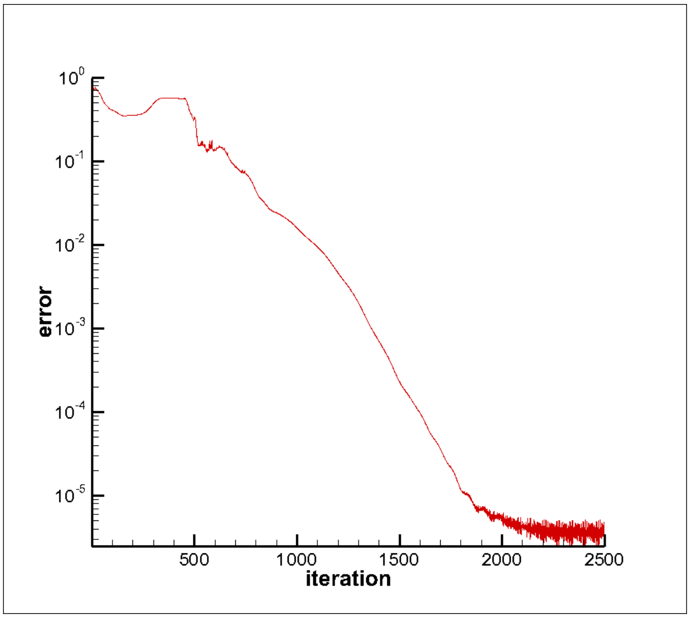

Figure 36 convergence history

4.2 Unsteady problems

4.2.1 moving sphere

in order to verify the meshless point generation technique for moving system, an analysis on the flow around moving sphere was carried out. For verification, the steady state result which has freestream Mach number 2 is selected as the reference. Then, three unsteady cases are carried out. They have three different Mach number of the sphere and three different freestream Mach number respectively. In all the unsteady case, freestream Mach number observed from the sphere is 2. The unsteady results are compared with the reference. It indicates that all cases have same result, because the relative velocity of the four cases is same. The information of the case is shown in the Table 4

	Freestream Mach number	Mach number of the sphere
Case 1	0.0	2.0
Case 2	1.0	1.0
Case 3	1.5	0.5
Case 4(reference)	2.0	0.0

Table 4 the outline of the unsteady problem (moving sphere)

The results are shown in Figure 37 and Figure 38. Figure 37 denotes the comparison of the pressure coefficient along *z=0*. It indicates that all cases have almost same pressure coefficient. Additionally, Figure 38 shows the comparison of the density contour. The shock of the two cases are almost same. These results verify that the point generation technique is available for the unsteady problem including moving boundary.

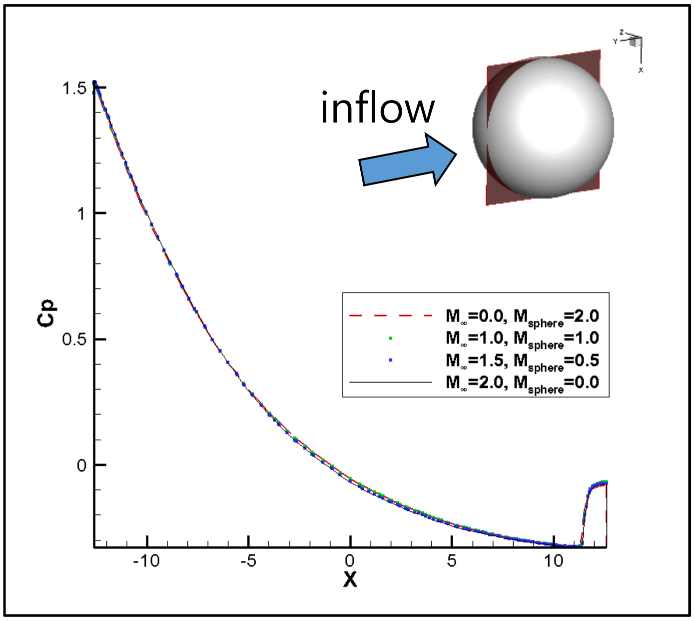

Figure 37 the comparison of the pressure coefficient

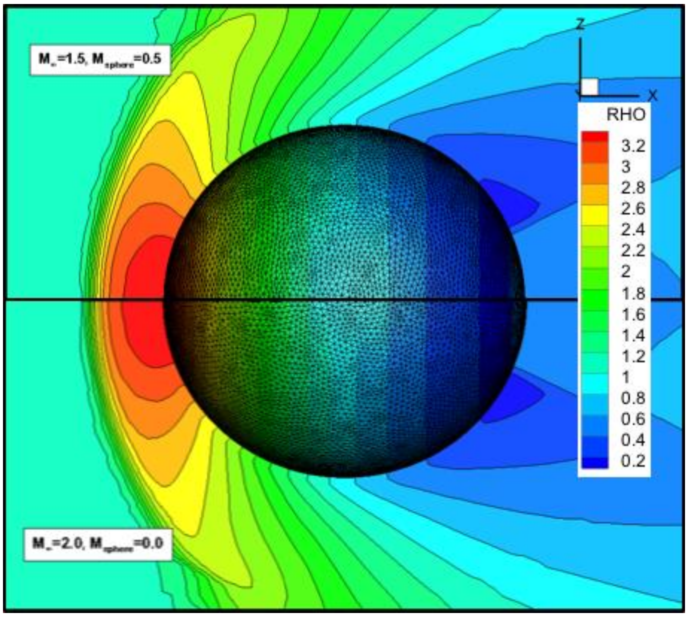

Figure 38 the comparison of the density contour

(upper : unsteady, nether : steady)

Chapter 5. Conclusions

In this study, the point generation technique was developed. Using hybrid of the near surface point system and the background point system, both the effectiveness and the accuracy were considered. Additionally, hybrid point system is useful for the moving point system. Through the developed technique, no matter how the geometry is complex, it is possible to generate the computational domain is easily using the developed method.

The three cases are carried out for validation. the first case is the space shuttle reentry simulation. This case verified the robustness of the point generation technique for the complex object which has both concave and convex geometry. Additionally, it is verified that the method is available to hypersonic region including highly strong shock. The second case is flow around the missile body. Because this model integrates the internal flow and the external flow, it can be considered as highly complicated geometry than Space shuttle. With successful analysis of the second case, the tremendous robustness of the point generation technique and the meshless method was verified. The last case is the flow around the moving sphere. This validation showed a success of expansion to unsteady region of the meshless point generation technique. Consequently, a result which has similar levels of accuracy can be obtained within a short time using the developed method.

Chapter 6. References

[1] Katz, Aaron, and Antony Jameson. "Edge-based meshless methods for compressible flow simulations." AIAA paper 699 (2008).

[2] Huh, J., K. Kim, and S. Jung. "Meshless Method for Simulation of 2-D Compressible Flow." The 2013 Asia-Pacific International Symposium on Aerospace Technology. (2013).

[3] S, Rhee, Huh, J, K. Kim, and S. Jung “Three dimensional meshless point generation technique for complex geometry” The World Congress on Aeronautics, Nano, Bio, Robotics, and Energy (ANBRE15) (2015)

[4] Huh, Jin Young, Kyu Hong Kim, and Suk Young Jung. "MESHLESS METHOD FOR SIMULATION OF COMPRESSIBLE REACTING FLOW." ICAS (2014)

[5] Mendez, B., and A. Velazquez. "Finite point solver for the simulation of 2-D laminar incompressible unsteady flows." Computer methods in applied mechanics and engineering 193.9 (2004): 825-848.

[6] Park C and Yoon S. Fully Coupled Implicit Method for Thermochemical Nonequilibrium Air at Suborbital Flight Speed, J. Spacecraft and Rockets, Vol. 28, No. 1, pp 31-39, 1991.

[7] Candler G V. The Computation of Weakly Ionized Hypersonic Flows in Thermo-Chemical Non equilibrium, Ph.D. Thesis, Stanford Univ., 1988.

[8] Donea, J., J-Ph Ponthot, and Antonio Rodriguez Ferran. "Encyclopedia of computational mechanics." (2004).

[9] Kim, Kyu Hong, Chongam Kim, and Oh-Hyun Rho. "Methods for the accurate

computations of hypersonic flows: I. AUSMPW+ scheme." Journal of Computational Physics 174.1 (2001): 38-80.

[10] Sridar, D., and N. Balakrishnan. "An upwind finite difference scheme for meshless solvers." Journal of Computational Physics 189.1 (2003): 1-29.

[11] Katz, Aaron, and Antony Jameson. "A comparison of various meshless schemes within a unified algorithm." AIAA paper 594 (2009).

[12] Yoon, Seokkwan, and Antony Jameson. "Lower-upper symmetric-Gauss-Seidel method for the Euler and Navier-Stokes equations." AIAA journal 26.9 (1988): 1025-1026.

[13] Chen, H. Q., and C. Shu. "An efficient implicit mesh-free method to solve two-dimensional compressible Euler equations." International Journal of Modern Physics C 16.03 (2005): 439-454.

[14] Mc Ghee, R. J. "Jet-plume-induced flow separation on axisymmetric bodies at Mach numbers of 3.00, 4.50, and 6.00." (1970).

[15] Burt Jr, James Robert. An Investigation of the Effectiveness of Several Devices in Simulating a Rocket Plume at Free Stream Mach Numbers 0.9 to 1.2. No. RD-TR-71-22. ARMY MISSILE COMMAND REDSTONE ARSENAL ALA AEROBALLISTICS DIRECTORATE, 1971.

[16] Jung, Suk-Young, and Sung-Joon Yoon. "Effects of Underexpanded Plume in Transonic Region on Longitudinal Stability." Journal of the Korean Society for Aeronautical & Space Sciences 32.8 (2004): 118-128.

국문 초록

본 연구에서는 무격자 유동해석 기법을 위한 질점 생성 프로그램을 개발하였다. 본 연구에서는 개발된 프로그램을 이용해 미사일 형상, 우주왕복선 형상 등 여러 복잡한 형상에 대해 computational domain 을 생성하였고, 생성된 domain 을 토대로 무격자 유동 해석을 수행하였다. 무격자 유동해석은 Huh 에 의해 개발된 무격자 유동해석 코드를 사용하였고, reference 는 본 연구실에서 개발된 Structured Finite Volume Method 결과로 하였다. 두 코드 모두 AUSMPW+ 를 Numerical Flux scheme 으로 사용하였고, 시간적분법은 LU-SGS, Limiter 는 Minmod 를 적용하였다. 수행된 결과 비교를 통해 무격자 질점 생성 기법과 유동해석 기법의 정확성와 효율성 강건성을 검증하였다. 따라서 본 연구에서 개발된 무격자 유동 해석 기법은 무격자 유동 해석 기법의 접근성 및 효율성 연구에 기여할 수 있을 것으로 판단된다.

주요어 : 무격자 기법, 질점 생성 기법, 비정상 유동 해석

학번 : 2014 – 20671

성명 : 이 재 상